Scientific Reports

https://doi.org/10.1038/s41598-026-44630-1

Article in Press

Daily transient analysis of an integrated solar-driven direct contact membrane distillation for cogeneration production of freshwater and electricity

Received: 16 December 2025

Accepted: 12 March 2026

Published online: 30 March 2026

Cite this article as: Salavat A.K. & Ziapour B.M. Daily transient analysis of an integrated solar-driven direct contact membrane distillation for cogeneration production of freshwater and electricity. *Sci Rep* (2026). https://doi.org/10.1038/s41598-026-44630-1

Ali Kiani Salavat & Behrooz M. Ziapour

Daily transient analysis of an integrated solar-driven direct contact membrane distillation for cogeneration production of freshwater and electricity

Ali Kiani Salavat*, Behrooz M. Ziapour*

Department of Mechanical Engineering, University of Mohaghegh Ardabili, Ardabil, Iran

*Corresponding authors: Alikiani333@gmail.com (Ali Kiani Salavat), Ziapourbm@uma.ac.ir (B.M. Ziapour),

Abstract

The rapid expansion of the world's population has made access to adequate freshwater supplies one of the most urgent global challenges. In response, the present work introduces a novel desalination system that couples a direct contact membrane distillation (DCMD) unit with a photovoltaic-thermal (PVT) collector, enabling simultaneous production of purified water and electricity from solar energy alone. The PVT collector integrates a photovoltaic panel with a thermal collector to simultaneously generate electricity and heat. The proposed system is transiently analyzed using Engineering Equation Solver (EES) software. This study investigates the effects of the PVT collector tilt angle and reflector inclination angles on system performance. Additionally, to gain a deeper understanding of system behavior and the influence of various design parameters, the impacts of collector area and coolant flow rate through the PVT module are examined. The results demonstrate that increasing the solar collector area has a positive effect on freshwater production, whereas increasing the coolant flow rate through the PVT module exhibits a negative impact on distillate yield. The overall energy efficiency of the system and the energy efficiency of the PVT collector are found to be 36.01% and 43.44%, respectively. Under baseline conditions, the proposed system produces 18.70 kg/day of

Keywords: Cogeneration system, Desalination, Direct contact membrane distillation, Numerical simulation, Photovoltaic-thermal system, Solar energy

1. Introduction

The relentless increase in global population, combined with widespread industrial development, has imposed severe strain on available freshwater supplies, rendering the development of sustainable desalination and purification methods an urgent priority. Among various renewable energy sources, solar energy stands out as a highly promising candidate due to its abundance, widespread availability, and environmental compatibility [1]. This introduction aims to highlight the beneficial and positive aspects of solar energy in the context of desalination and distillation, thereby providing an overview of its applications in these critical water treatment processes.

Abundance and renewability: Solar energy is virtually inexhaustible, with approximately 173,000 terawatts of solar radiation continuously reaching the Earth's surface [2]. This abundance makes it an attractive option for desalination and distillation plants that can operate as long as sunlight is available.

Environmental friendliness: Unlike fossil fuels, solar energy generation emits no greenhouse gases or pollutants, contributing to a cleaner environment and helping mitigate climate change [2]. This is particularly significant for desalination facilities, which can otherwise have considerable environmental impacts if not operated sustainably.

Versatility: Solar energy can be harnessed in multiple forms, including thermal and photovoltaic, enabling the development of diverse desalination and distillation technologies such as solar stills, solar-driven MD, and photovoltaic-powered reverse osmosis systems [2].

Decentralization: Solar energy systems can be deployed at small scales, facilitating decentralized water treatment solutions that are especially valuable for remote and rural areas lacking access to centralized water supply infrastructure [2].

Membrane distillation (MD) is a thermally driven separation technique in which vapor generated from a liquid feed migrates through the pores of a hydrophobic microporous membrane, enabling the isolation of volatile components from non-volatile ones [3]. Owing to its effectiveness in seawater and brackish water desalination, reclamation of industrial wastewater, and concentration of thermolabile substances, MD has emerged as a highly promising alternative to traditional separation processes [3].

Energy efficiency: MD operates at lower temperatures than traditional distillation, significantly reducing energy consumption—particularly when integrated with renewable energy sources [4].

High product quality: The hydrophobic nature of the membrane allows only vapor to pass through, resulting in distillate of exceptionally high purity [4].

Robustness: MD membranes can tolerate high salinity levels and are less prone to fouling compared to pressure-driven membrane processes [4].

Versatility: MD can be applied across a wide range of industrial and environmental applications, including brine concentration, pharmaceutical production, and food processing [4].

Ahmadi et al. [5] investigated and optimized a vacuum-MD system powered by solar energy. Their system, utilizing a 6 m^2 solar collector, achieved an optimum daily production of 92.5 kg of purified water.

1.1. Literature review

Global water scarcity, exacerbated by population growth, climate variability, and uneven resource distribution, has propelled the search for sustainable purification methods [6]. Solar-driven desalination emerges as a viable pathway, leveraging abundant renewable energy to convert saline or brackish sources into potable supplies without heavy reliance on fossil fuels [7]. This review synthesizes advancements in solar-integrated membrane distillation (MD) systems, with a particular emphasis on photovoltaic-thermal (PVT) hybrids [8]. It traces historical developments, evaluates configuration-specific performances, and identifies persistent barriers, drawing from studies published between 2020 and 2025 to underscore the trajectory toward efficient, off-grid solutions.

The journey of solar desalination traces back to rudimentary passive devices that harness natural evaporation under transparent covers [10]. These basin-style setups, while low-cost and maintenance-free, suffer from sluggish vapor generation rates tied to diurnal solar cycles and ambient humidity, rendering them inadequate for large-scale needs. Transitioning to active paradigms, researchers incorporated concentrating mirrors or tracking mechanisms to amplify thermal input, yielding modest gains in productivity but introducing mechanical vulnerabilities [13]. By the early 2020s, flat-plate collectors became staples, channeling low-to-medium heat (50–80°C) to evaporation chambers, thus stabilizing output amid fluctuating irradiance. Yet, these thermal-centric designs largely sidelined electrical co-generation, a shortfall in powering ancillary operations like circulation pumps [12].

MD distinguishes itself as a thermally activated process, where a vapor pressure differential across a non-wetting porous barrier propels phase-selective transport [13,14]. Unlike pressure-intensive alternatives such as

reverse osmosis, MD thrives on waste or low-grade heat, aligning seamlessly with solar intermittency. Its core appeal lies in near-complete solute rejection (>99%) for brines up to hypersalinity levels, coupled with fouling resilience from the hydrophobic interface. Configurations vary: direct contact MD (DCMD) employs adjacent liquid streams for straightforward heat exchange, promoting high flux but risking internal leaks; vacuum MD (VMD) employs suction to lower boiling points, accelerating permeation at the expense of vacuum upkeep [12]; air-gap MD (AGMD) interposes a stagnant air layer to curb conductive losses, enhancing insulation yet curbing convective momentum [15].

Solar augmentation of MD gained momentum post-2020, with collectors preheating feeds to sustain transmembrane gradients [13]. Initial explorations paired evacuated tube arrays with VMD modules, revealing flux elevations proportional to inlet temperatures (typically 60–70°C), though vacuum auxiliaries inflated energy footprints [12]. AGMD pairings with parabolic troughs mitigated nocturnal cooldowns via insulated gaps, fostering overnight carryover, but air entrapment often throttled mass throughput by 20–30% relative to DCMD [15]. These hybrids underscored MD's adaptability to solar's diffuse nature, slashing operational costs by repurposing thermal rejects, yet steady-state assumptions in early models masked real-time dips from cloud cover or dust accumulation [11].

PVT collectors revolutionized this landscape by fusing photovoltaic cells atop thermal absorbers, mitigating PV efficiency drops (0.4–0.5% per °C rise) through active cooling while harvesting the extracted warmth for downstream uses [8]. This symbiotic architecture boosts areal yields, converting up to 70% of incident photons into usable forms versus 15–20% for PV alone. In desalination contexts, PVT effluent—tempered to MD-optimal ranges—fuels vaporization, with surplus electrons energizing system peripherals [9,16]. Pioneering integrations circa 2022 demonstrated PVT-DCMD prototypes yielding dual streams: modest electricity (50–200 W/m^2) alongside distillate rates scaling with glazing transmittance [15].

A cluster of 2024–2025 investigations illuminated PVT-MD dynamics [9]. One modeling effort simulated a PVT-DCMD cascade under varying climes, projecting enhanced daily outputs from optimized apertures, with thermal yields around mid-50% and electrical near 11%, contingent on feed velocities below certain thresholds to preserve outlet heats [9]. Optimization routines therein pinpointed tilt angles (30–40°) for maximal insolation capture, though high flows eroded gradients, reducing permeation [8]. Complementarily, a prototype blueprint for PVT-forward osmosis-MD hybrids advocated modular scaling for rural deployments, emphasizing draw solution

recycling to amplify recoveries, albeit at the cost of osmotic priming complexity [7].

Reflectors and nanofluid enhancements further refined PVT outputs [16]. Studies incorporating specular boosters reported irradiance uplifts, translating to sustained DCMD fluxes amid seasonal lulls, but angular misalignment halved gains, urging adaptive tracking [8]. Nanofluid-infused circuits, blending alumina or graphene oxides, escalated convective coefficients, curbing polarization layers and elevating overall utilizations [16]. Economic dissections pegged levelized costs lower for PVT-MD compared to grid-tied alternatives in sun-rich locales, inclusive of long-term lifespans [16].

Notwithstanding strides, lacunae persist [13]. Transient analyses remain sparse; most validations lean on hourly averages, underplaying sub-minute irradiance spikes that could spike thermal stresses or flux instabilities [17]. Fouling kinetics, especially in protracted brines, evade rigorous quantification, with bio-growth models lagging behind inorganic scalants [14]. Cogeneration metrics often isolate electrical from thermal audits, obscuring holistic efficiencies under load mismatches—e.g., daytime surpluses versus evening deficits [9]. Scalability hurdles loom for community arrays, where land footprints and material sourcing clash with arid topographies. Environmental audits, though nascent, flag microplastic leachates from degraded membranes and avian hazards from concentrators, mandating lifecycle baselines [13].

Comparative lenses reveal DCMD's edge in operational ease over VMD's vacuum rigors, though the latter suits hypersaline feeds via enhanced Knudsen regimes [12]. AGMD curtails energy leaks but lags in throughput, ideal for purity-centric niches [15]. PVT hybrids eclipse standalone solar thermal by embedding power autonomy, yet demand sophisticated controls to avert PV hotspots [6]. Multi-effect MD extensions with PVT recycle cascades, reclaiming latent loads, but cascade plumbing inflates upfronts [11].

Emergent motifs pivot toward intelligent hybrids: AI-orchestrated flows to preempt polarization, or advanced tandems for spectral splitting [13]. Bibliometric sweeps forecast a surge in PVT-MD research, propelled by sustainability alignments [6].

In essence, solar PVT-MD synergies forge a resilient bulwark against hydric deficits, melding thermal prowess with electrical versatility [8]. This corpus, spanning conceptual blueprints to field trials, affirms viability but clamors for dynamic, fouling-resilient paradigms. The ensuing inquiry

bridges these voids via transient simulations of reflector-augmented PVT-DCMD, probing tilt-flow interplays for optimized co-yields.

Table 1
Overview of Selected Recent Investigations on Solar and PVT-Driven Membrane Distillation Systems

Study Focus	Key Contributions	Limitations	Comparison to Other Approaches
Passive solar stills and early active collectors [11]	Established foundational evaporation under covers; introduced tracking for thermal boosts.	Output variability with weather; no electrical co-output.	Simpler than MD but lower yields; precursor to PVT for heat-only ops.
VMD-solar integrations [12]	Vacuum-aided flux in tube collectors; steady thermal drives.	Pressure maintenance overheads; steady-state biases.	Fluxier than DCMD but energy-hungry; less autonomous than PVT hybrids.
AGMD with insulation gaps [15]	Reduced conduction losses; brine tolerance.	Air drag on vapor; scaled setups.	Insulation beats DCMD leaks but throttles rates; pairs well with low-heat PVT.
Basic PVT thermal modeling [6]	Dual energy capture; waste heat repurposing.	Overlooked transients; fixed geometries.	Outstrips PV alone in utilization; bridges to MD for desalination synergy.
PVT-DCMD simulations [9]	Flux predictions; efficiency mappings under varying conditions.	Flow-velocity trade-offs underexplored in some cases.	More predictive than prototypes; enhances over non-hybrid MD.

Study Focus	Key Contributions	Limitations	Comparison to Other Approaches
Reflector-enhanced PVT [9]	Irradiance amplification; angular optima.	Misalignment sensitivities; no fouling ties.	Boosts input vs. standard PVT; complements DCMD for variable suns.
Nanofluid PVT-MD pilots [16]	Convective uplifts; cost audits.	Fluid stability issues; prototype scales.	Greener than base fluids; rivals multi-effect in recovery sans complexity.

This tabular synopsis clusters inquiries by motif, distilling merits, constraints, and relational standings sans specific metrics. Passive baselines yield to active evolutions, with PVT-DCMD exemplars spotlighting integration apexes [8]. Collective frailties—like transience neglect—illuminate niches for holistic, adaptive designs herein pursued.

Although various configurations of solar-driven membrane distillation systems have been previously investigated, the present study distinguishes itself in several key aspects. Unlike most prior works that rely on steady-state or time-averaged analysis, this study performs a fully transient daily simulation under realistic solar irradiance conditions. In addition, the combined effects of collector tilt angle and dual-reflector inclination angles on both thermal and electrical performance are systematically analyzed, which has not been adequately addressed in previous PVT–MD studies. Furthermore, the focus on a direct contact membrane distillation configuration enables system simplicity while providing a comprehensive trade-off analysis between freshwater production and electrical efficiency. These features collectively define the novelty and practical relevance of the present work.

2. Process Description

Fig. 1 illustrates a fully integrated, off-grid solar desalination system that simultaneously generates electricity and fresh water using a hybrid photovoltaic-thermal (PVT) collectors coupled with a direct contact membrane distillation (DCMD) module.

The PVT collector operates as the sole energy supplier for the entire process. Incident solar irradiance (I_0) first passes through a glass cover and reaches the photovoltaic layer. The solar cells convert a portion of the incoming radiation directly into DC electricity, while the remaining energy is transformed into heat. This heat, which would otherwise reduce photovoltaic efficiency, is actively captured by an absorber plate bonded to a network of fluid channels. Saline or brackish feed water, initially at ambient temperature, flows beneath the absorber plate in a serpentine or parallel-flow arrangement. As the water travels along the collector length, it absorbs thermal energy and exits at an elevated temperature, typically in the range of 60–80 °C, depending on solar intensity, flow rate, and ambient conditions.

The preheated saline stream is then pumped into the hot-side (feed) channel of the DCMD module. The DCMD unit consists of a hydrophobic microporous membrane that separates two counter- or co-flowing liquid streams maintained in direct contact with the membrane surfaces. On the opposite side of the membrane, a cooler distillate stream circulates through the permeate channel. The temperature difference across the thin membrane establishes a vapor pressure gradient that serves as the only driving force for mass transfer. Water molecules evaporate at the warm feed–membrane interface, diffuse as vapor through the air-filled pores, and condense immediately upon reaching the cold permeate–membrane interface. Dissolved salts and non-volatile contaminants are effectively rejected by the hydrophobic membrane, resulting in high-purity distillate.

The cold permeate loop is designed as a closed circuit. A portion of the permeate stream is continuously withdrawn as product water and directed to a storage tank, while the remaining flow is recirculated. To sustain the required temperature difference, heat is rejected from the permeate loop through an air-cooled or water-cooled heat exchanger before re-entering the DCMD module. The concentrated brine stream exits the feed channel at the bottom of the module and is either discharged or further processed.

In summary, the proposed configuration represents a compact, modular, and completely autonomous solution that converts a single solar input into two valuable outputs (electricity and fresh water) while requiring minimal maintenance and no chemical pretreatment of the feed water.

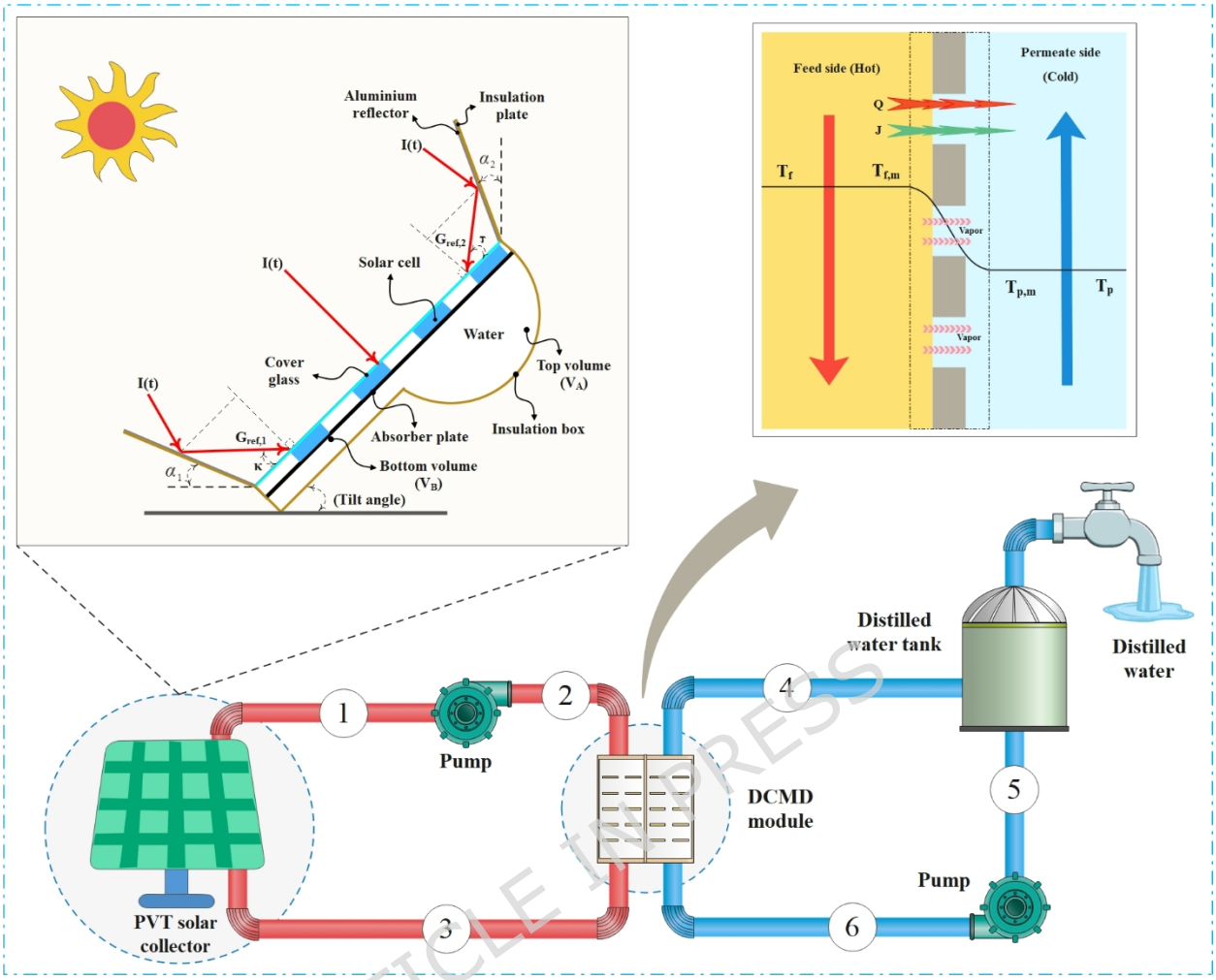

Fig. 1. Schematic diagram of the proposed system.

2.1. Photovoltaic-Thermal (PVT) System

Fig. 2 presents a schematic representation of the photovoltaic-thermal collector equipped with reflectors. The PVT collector consists of a cover glass, a photovoltaic module, a flat-plate absorber, an insulated enclosure (constructed with rock wool insulation), a stratified dual-section water storage tank, and two identical flat aluminum reflectors mounted at the rear of the insulated enclosure. The lower reflector forms an angle α_1 with the horizontal plane, whereas the upper reflector forms an angle α_2 with the vertical plane. During energy collection periods, both reflectors can be rotated to fully expose the collector's glass cover, which serves as a transparent insulating layer. The key assumptions adopted for the PVT system are as follows:

1. Heat input to the collector is considered one-dimensional, whereas heat losses are treated as three-dimensional (Fig. 1).
2. Natural convection within the water storage tank is taken into account.
3. No thermal stratification is assumed in the water storage tank. The storage tank is assumed to have a uniform temperature distribution. This simplification is supported by the relatively small tank volume, continuous fluid circulation, and mixing effects induced by the feed loop, which collectively reduce temperature gradients inside the tank.
4. The heat capacity of the PVT collector components is neglected compared to the heat capacity of the stored water.
5. All rays reflected by each reflector are assumed to fully and uniformly irradiate the absorber surface; thus, the reflector area is sufficiently large.
6. The entire PVT system operates under quasi-steady-state conditions. Although the overall system performance is evaluated under transient daily solar conditions, the PVT collector is assumed to operate in a quasi-steady manner within each simulation time step. This assumption is justified because the thermal response time of the collector components is much shorter than the simulation time interval, allowing each time step to be treated as locally steady while still capturing the time-varying nature of solar irradiance and ambient conditions.

2.2. DCMD System

In direct contact membrane distillation, temperature polarization causes the actual temperatures at the feed-side and permeate-side vapor–liquid interfaces to deviate significantly from the measured bulk temperatures of the respective streams. The resulting temperature drop across each liquid boundary layer establishes a transmembrane partial vapor pressure gradient across the hydrophobic microporous membrane, which serves as the sole driving force for vapor transport in the DCMD process.

As depicted in Fig. 3, water vapor migrates through the open pores of the hydrophobic membrane, while heat is transferred concurrently via three distinct pathways: (i) conduction through the membrane matrix and trapped gas, (ii) latent heat carried by the permeating vapor, and (iii) convective exchange across the thermal boundary layers formed on both the feed and permeate sides of the membrane.

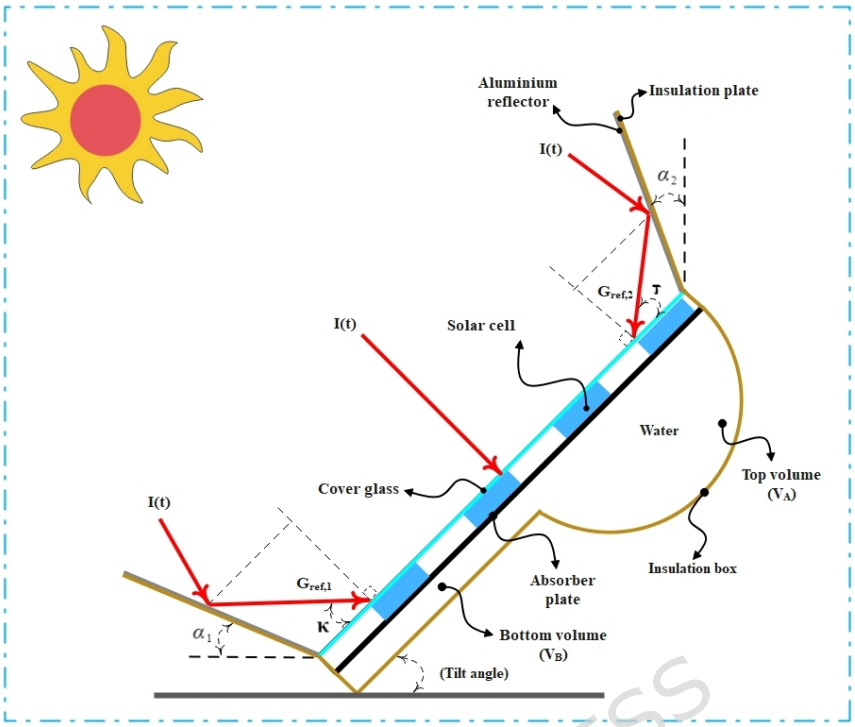

Fig. 2. Proposed configuration of the photovoltaic-thermal collector.

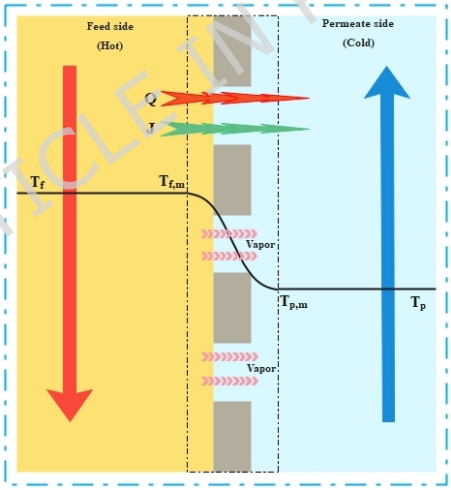

Fig. 3. Schematic representation of the heat and mass transfer mechanisms in the DCMD process.

3. Governing equations

3.1. Photovoltaic-thermal modeling

The energy equation for the solar collector is obtained from the following equations [18]:

For the photovoltaic system we have:

$$\tau_g \alpha_{sc} \beta_{sc} G_t(t) WL = U_{tc.a}(T_{sc} - T_{amb})WL + U_T(T_{sc} - T_{bs})WL \quad (1)$$

Here, $G_t(t)$ represents the total solar radiation intensity, which is as follows:

$$G_t(t) = I(t) + G_{ref.1} + G_{ref.2} \quad (2)$$

Here, $G_{ref,1}$ and $G_{ref,2}$ represent the solar radiation reflected from the reflectors, which are obtained from the following equations [18]:

$$G_{ref,1} = \rho_{al} I(t).\sin(\kappa).\sin\left[\frac{\pi}{2} - (\beta + \alpha_1)\right] \quad (3)$$

$$\kappa = 2(\beta + \alpha_1) - \frac{\pi}{2} \quad (4)$$

This equation calculates the intensity of radiation reflected by the lower reflector. ρ_{al} is its reflectance coefficient and α_1 is the angle of the lower reflector with respect to the horizontal surface. This equation shows how the angle of the reflector affects the amount of energy reflected to the panel [18].

$$G_{ref,2} = \rho_{al} I(t).\sin(\tau).\sin\left[\frac{\pi}{2} + (\alpha_2 - \beta)\right] \quad (5)$$

$$\kappa = \frac{\pi}{2} + 2(\alpha_2 - \beta) \quad (6)$$

For the back of the absorber plate, we have [18]:

$$U_T(T_{sc} - T_{bs})WL + \tau_g \alpha_{abs}(1 - \beta_{sc}) G_t(t) WL = k_1 h_f (T_{bs} - T_f) \quad (7)$$

Eq. (5) expresses the energy equation for the back of the photovoltaic absorber plate, where τ_g is the glass transmittance, α_{abs} is the absorptivity of the plate, and β_{SC} is the solar cell packing factor.

For water storage in the tank, we have [18]:

$$k_1 h_f (T_{bs} - T_f) A_{bs} = U_{Loss} A_{ins}(T_f - T_{amb}) + M_f C_f \frac{dT_f}{dt} \quad (8)$$

Here k_1 is defined as $k_1 = \eta(\frac{A_o}{A_c})$[20].

$$T_f = \frac{f(t)}{a}[1 - \exp(-at) + T_{fi}\exp(-at)] \quad (9)$$

Solving eq. (6), with initial conditions at t = 0, $T_f = T_{fi}$, we have [18]:

$$a = \frac{1}{M_f C_f}\left[U_{loss}A_{ins} + h_f A_{bs} - \frac{(k_1 h_f)^2 A_{bs}(U_{tc,a} + U_T)}{(k_1 h_f + U_T)(U_{tc,a} + U_T) - (U_T)^2}\right] \quad (10)$$

$$f(t) = \frac{1}{M_f C_f}$$
$$\left[U_{Loss}A_{ins}T_{amb} + k_1 h_f A_{bs}\frac{U_T(\alpha\tau)_{1,eff}G_t(t) + U_T U_{tc,a}T_{amb} + (\alpha\tau)_{2,eff}(U_{tc,a} + U_T)G_t(t)}{(k_1 h_f + U_T)(U_{tc,a} + U_T) - (U_T)^2}\right] \quad (11)$$

$$U_{tc,a} = \left[\frac{L_g}{k_g} + \frac{1}{h_{g\text{-}amb} + h_{r\text{-}sky}}\right]^{-1} \quad (12)$$

Eq. (10) calculates the overall heat transfer coefficient ($U_{tc,a}$) between the solar cells and the environment. The overall thermal resistance consists of two parts: the conductive resistance in the cover glass (k_g/L_g), which depends on the thickness (L_g) and thermal conductivity of the glass (k_g), and the convective and radiative resistance to the environment ($\frac{1}{h_{g\text{-}amb} + h_{r\text{-}sky}}$), where $h_{g\text{-}amb}$ is the convection coefficient to the environment and $h_{r\text{-}sky}$ is the radiation coefficient to the sky [18].

$$U_T = \left[\frac{L_{abs}}{k_{abs}} + \frac{L_{sc}}{k_{sc}}\right]^{-1} \quad (13)$$

Eq. (10) calculates the effective heat transfer coefficient (U_T) between the absorber plate and the solar cells, which is used in Eq. (5). The total thermal resistance consists of the conductive resistance in the absorber plate (L_{abs}/k_{abs}) and the solar cells (L_{sc}/k_{sc}), which depends on the thickness (L_{abs}, L_{SC}) and thermal conductivity (k_{abs}, k_{sc}) of these layers [18].

$$U_{Loss} = \left[\frac{L_{ins}}{k_{ins}} + \frac{1}{h_{amb}}\right]^{-1} \quad (14)$$

Eq. (12) calculates the heat loss coefficient (U_{Loss}) from the storage tank to the environment, which is used in Eq. (6). The total thermal resistance includes the conductive resistance in the insulation layer (L_{ins}/k_{ins}), which depends on the thickness (L_{ins}) and thermal conductivity (k_{ins}) of the insulation.

3.2. Mass transfer in a DCMD system

The mass transfer mechanism in MD proceeds through three consecutive stages: (i) evaporation of water molecules from the hot feed solution at the membrane–liquid interface on the feed side, (ii) diffusion of the generated vapor through the microporous structure of the hydrophobic membrane, and (iii) immediate condensation of the transported vapor at the membrane–liquid interface on the cold permeate side [7]. In DCMD system, the transmembrane mass flux is directly governed by the vapor pressure difference established across the membrane and is expressed by the relation presented in [20].

$$J = D_e.\Delta P_m = D_e(p_{m.f} - P^0_{m.p}) \quad (15)$$

Here J denotes the transmembrane permeate flux ($kg \cdot m^{-2} \cdot s^{-1}$), De represents the effective vapor diffusion coefficient within the membrane pores, and $P_{m,f}$ and $P_{m,p}$ correspond to the partial vapor pressures of water at the feed-side and permeate-side membrane surfaces, respectively. These interfacial partial pressures are determined under the assumption of local vapor–liquid equilibrium at each membrane surface [19]. On the feed side, the presence of dissolved NaCl reduces the vapor pressure relative to pure water; therefore, a salinity-dependent correction must be applied when evaluating $P_{m,f}$ [19].

$$p_{m.f} = P^0_{m.p} \times X_{w.f} \times a_{w.f} \quad (16)$$

$X_{w,f}$ denotes the mole fraction of water in the feed solution, while X_{NaCl} represents the mole fraction of dissolved sodium chloride. The symbol $a_{w,f}$ stands for the activity of water in the NaCl solution, which is calculated using the relation provided in the original source [19].

$$a_{w.f} = 1 - 0.5X_{Nacl} - 10(X_{Nacl})^2 \quad (17)$$

The terms $P^0_{m,f}$and $P^0_{m,p}$ denote the partial pressures of pure water vapor on the feed-side and permeate-side interfaces of the membrane, respectively. These values are determined through the Antoine correlation, using the corresponding interface temperatures $P^0_{m,f}$and $P^0_{m,p}$.

$$P^0_{m.f} = \exp\left(23.1964 - \frac{3816.44}{T_{m.f} - 46.13}\right) \quad (18)$$

$$P^{0}_{m.p} = \exp\left(23.1964 - \frac{3816.44}{T_{m.p} - 46.13}\right)$$
(19)

Vapor transport through the microporous hydrophobic membrane can occur via three fundamental mechanisms: Knudsen diffusion, ordinary molecular diffusion, and viscous (Poiseuille) flow. In DCMD system, however, viscous flow is negligible because both the feed and permeate streams are maintained at essentially atmospheric pressure (~1 atm), resulting in no significant hydrostatic pressure gradient across the membrane.

Consequently, mass transfer is governed solely by the interplay between Knudsen diffusion and ordinary molecular diffusion. The dominant regime is determined by the relative magnitude of the mean free path of water vapor molecules compared to the membrane pore diameter. A transition parameter α ($0 \leq \alpha \leq 1$) is introduced to quantify the contribution of each mechanism, where $\alpha = 0$ corresponds to pure molecular diffusion and $\alpha = 1$ indicates purely Knudsen-controlled transport [21].

$$D_e = \left[\frac{\alpha}{D_k} + \frac{1-\alpha}{D_M}\right]^{-1}$$
(20)

The symbols D_e, D_K, and D_M stand for the overall diffusion coefficient, the Knudsen diffusion term, and the ordinary molecular diffusion term, respectively. The expressions for D_e, D_K, and D_M are provided in the relations below, as outlined in reference [5].

$$D_K = \left[\left(\frac{3\phi}{2\times\epsilon\times d_{pore}}\right)\times\left(\frac{\pi\times R_g\times T_m}{8M_{wt}}\right)\right]$$
(21)

$$D_M = \left[\frac{R_g\times T_m\times P\phi}{M_{wt}\times\epsilon\times PD_{WA}}\right]$$
(22)

In the above expressions, ϕ represents the membrane tortuosity (accounting for the actual path length of vapor molecules through the porous structure), ϵ denotes the membrane porosity, R_g is the universal gas constant, T_m is the mean temperature at the two membrane interfaces, d_{pore} is the mean pore diameter, M_{wt} is the molar mass of water, P is the total gas pressure within the pores (taken as atmospheric pressure, since it equals the sum of the partial pressures of entrapped air and water vapor), and PD_{WA} is the binary diffusion coefficient of water vapor in air.

The water–air diffusivity PD_{WA} (expressed in $Pa\cdot m^2/s$) is evaluated as a function of temperature using the empirical correlation provided in [9], which remains valid over the temperature interval of 273–373 K.

$$PD_{WA} = 1.895 \times 10^{-5} \times T_m^{2.072} \quad (23)$$

$$T_m = \frac{T_{m.f} + T_{m.p}}{2} \quad (24)$$

The effective diffusion path length across the membrane is defined as $\phi = \delta \cdot \tau$, where δ stands for the membrane thickness (typically treated as a fixed value) and τ denotes the tortuosity factor (also considered constant). The tortuosity is commonly correlated with the membrane porosity ϵ through the Mackie–Mears relationship [22].

$$\tau = \frac{(2-\epsilon)^2}{\epsilon} \quad (25)$$

During prolonged desalination operation, salt ions gradually accumulate at the feed-side membrane surface, giving rise to the phenomenon known as concentration polarization. This effect is quantified by the concentration polarization factor (ζ), which is expressed as the ratio of the salt concentration at the feed-side membrane interface ($C_{m,f}$) to the salt concentration in the bulk feed stream ($C_{b,f}$):

$$\zeta = \frac{C_{m.f}}{C_{b.f}} \quad (26)$$

The salt concentration at the feed-side membrane interface ($C_{m,f}$) is calculated using the correlation proposed by Martínez and Vázquez [22].

$$C_{m,f} = C_{b.f} \times \exp\left(\frac{J}{K_s \times \rho}\right) \quad (27)$$

Here, J represents the mass flux across the membrane, while k_s denotes the coefficient governing the convective transfer of dissolved solids in the boundary layer [22].

$$k_s = \frac{Sh \times D_e}{D_h} \quad (28)$$

3.3. Heat transfer in a DCMD system

Heat transfer occurs in three stages:

3.3.1. Heat transfer from the feed side to the membrane surface

The convective mode dominates thermal energy movement within the boundary layer on the feed side, and this process is formulated according to the standard convective heat transfer relation, as detailed in reference [23]:

$$Q_f = h_f(T_{b.f} - T_{m.f})$$
(29)

Here, Q_f represents the convective heat transfer rate per unit area (W/m^2) from the bulk feed stream to the membrane surface, $T_{b,f}$ is the bulk feed temperature (taken as the arithmetic mean of the inlet and outlet temperatures on the hot side), and h_f denotes the convective heat transfer coefficient within the thermal boundary layer on the feed side of the membrane.

The convective heat transfer coefficient is determined using established empirical relations that rely on key dimensionless parameters, namely the Nusselt, Reynolds, and Prandtl numbers, as reported in reference [22]:

$$h_f = \frac{Nu \times k}{D_h}$$
(30)

In this context, k refers to the mean thermal conductivity of the working fluid adjacent to the feed-side surface of the membrane, whereas Nu stands for the Nusselt number. For conditions characterized by laminar regime, the Nusselt number is calculated using the relation presented below [22]:

$$Nu = 1/86 * \left(Re_0 \times Pr \times \frac{D_h}{L}\right)^{\frac{1}{3}}$$
(31)

Where Pr is the Prandtl number:

$$Pr = \frac{\mu \times C_p}{k}$$ (32)

3.3.2. Heat transfer through the membrane layer

The overal heat flux through the membrane (Q_m) arises from the combination of two contributions: pure conduction across the membrane material and entrapped gas (Q_C) and the latent heat carried by the vapor migrating through the pores (Q_v) [23]:

$$Q_C = \frac{k_m}{\delta}(T_{m.f} - T_{m.p})$$
(33)

$$Q_v = J \times \Delta H_v$$
(34)

Where k_m denotes the effective thermal conductivity of the membrane, which accounts for heat conduction through both the vapor–air mixture filling the pores (with thermal conductivity k_g) and the solid polymer matrix (with thermal conductivity k_s). This composite conductivity is evaluated using the relation provided below [23]:

$$k_m = \left[\frac{\epsilon}{k_g} + \frac{1-\epsilon}{k_s}\right]^{-1}$$
(35)

In this expression, δ denotes the thickness of the membrane layer, while ΔH_v represents the latent heat required for phase change of water from liquid to vapor. An approximation for this latent heat value is provided by the subsequent correlation [23]:

$$\Delta Hv = 1.7535\, T_{m.f} + 2024.3$$
(36)

Therefore, the total heat transfer through the membrane is [23]:

$$Q_m = Q_C + Q_v$$
(37)

$$Q_m = \frac{k_m}{\delta}(T_{m.p} - T_{m.f}) + J\Delta H_v$$
(38)

3.3.3. Heat transfer from the membrane surface to the permeate stream

Heat transfer across the boundary layer from the membrane surface on the infiltration side to the percolation stream is carried out by convection [23]:

$$Q_p = h_p(T_{m.p} - T_{b.p}) \quad (39)$$

where $T_{b,p}$ is the bulk permeate temperature (calculated as the arithmetic mean of the cold-side inlet and outlet temperatures) and h_p is the convective heat transfer coefficient in the permeate-side boundary layer, which is determined using an analogous approach to that employed for the feed side.

In DCMD system, the temperatures at the feed-side membrane interface ($T_{m,f}$) and the permeate-side membrane interface ($T_{m,p}$) are not directly measurable and must be determined iteratively. Under steady-state conditions, the overall heat flux crossing the DCMD module remains constant across all layers and is formulated as follows [23]:

$$Q_f = Q_m = Q_p$$
(40)

Combining eqs. (17), (36), and (37) leads to the following [19]:

$$T_{m.f} = \frac{k_m\left(T_{b.p} + \frac{h_f}{h_p}T_{b.f}\right) + \delta(h_f T_{b.f} - J\Delta H_v)}{(k_m) + h_f(\delta + \frac{k_m}{h_p})}$$
(41)

$$T_{m.p} = \frac{k_m\left(T_{b.f} + \frac{h_f}{h_p}T_{b.p}\right) + \delta(h_p T_{b.p} - J\Delta H_v)}{(k_m) + h_p(\delta + \frac{k_m}{h_f})}$$

(42)

3.4. Thermal efficiency of photovoltaic panel and thermal efficiency of the whole cycle

The relationship of the temperature-dependent overall thermal efficiency of the photovoltaic-thermal system can be presented as follows [25]:

$$\eta_{th,PVT} = \frac{M_f C_f (T_f^t - T_t^0)}{A_c \int_0^t I(t).dT}$$

(43)

Here, T_t^0 represents the water temperature inside the storage tank at the beginning of the simulation period (t = 0, corresponding to 8:00 a.m.), whereas T=t denotes the instantaneous tank water temperature at any subsequent time step t (e.g., 8:01 a.m., 10:00 a.m., 11:30 a.m., 14:45 p.m., 17:00 p.m., etc.).

Accordingly, the overall energy efficiency of the photovoltaic-thermal system is expressed by the following relation [18]:

$$\eta_{PVT} = \eta_{sc} + \eta_{th}$$

(44)

Where η_{SC} denotes the instantaneous overall electrical efficiency of the PVT module, which varies with operating temperature and is determined using the relation presented below [18]:

$$\eta_{sc} = \frac{\int_0^t \eta_{sci}.dT}{t}$$

(45)

For the total cycle thermal efficiency:

$$\eta_{th} = \eta_{PVT} + \frac{\dot{m}_{Freshwater} * h_{fg}}{\dot{Q}_m}$$

(46)

Despite the robustness of the numerical framework, certain limitations should be acknowledged. The simulations are conducted using Engineering Equation Solver (EES), which assumes quasi-steady behavior of system components within each time step. Long-term effects such as membrane fouling, scaling, and material degradation are not considered. In addition,

idealized heat transfer correlations and uniform flow distribution are assumed, which may introduce deviations under real operating conditions. Nevertheless, these assumptions are commonly adopted in early-stage system-level analyses and do not undermine the comparative trends and design insights obtained in this study.

4. Results and Discussion

4.1. Model Validation

To validate the performance of the photovoltaic-thermal (PVT) collector, the results obtained in the present study are compared with those reported in the reference study [25]. The solar irradiance and ambient temperature profiles used as input data are presented in Fig. 4. Fig. 5 compares the temperature predictions of the present work with those of [25], along with the relative error percentage. The maximum relative error is found to be less than 6%. Table 2 summarizes the key input parameters and operating conditions used for model validation, along with the corresponding reference data adopted from the literature. These parameters were selected to closely match previously reported experimental or numerical studies in order to ensure a consistent basis for comparison. Table 2 facilitates direct evaluation of the agreement between the present model predictions and validated results under comparable thermal and flow conditions.

Fig. 6 shows the validation of the DCMD module, where permeate flux is plotted against feed temperature. The maximum relative error occurs at a feed temperature of 45 °C and is approximately 7%, which confirms the acceptable accuracy of the developed DCMD model.

The minor deviations observed between the present model and the reference data can be attributed to several factors. First, slight discrepancies in solar irradiance and ambient temperature inputs may arise due to temporal resolution differences between measured and interpolated data. Second, the present model assumes uniform material properties and quasi-steady-state behavior of the PVT collector, whereas experimental systems inevitably experience transient thermal inertia and localized heat losses. For the DCMD module, deviations are mainly associated with simplifications in membrane properties, such as constant porosity and tortuosity, as well as uncertainties in estimating convective heat and mass transfer coefficients under different flow regimes. Furthermore, experimental measurements inherently involve sensor inaccuracies and unavoidable heat losses to the surroundings. Nevertheless, the relative errors remaining below 6% for the PVT system and

7% for the DCMD module confirm the reliability and robustness of the proposed numerical model.

4.2. Effect of Reflector Angles on Total Absorbed Irradiation

Fig. 7 shows the effect of the angles of placement of aluminum reflectors on the total radiation absorbed by the solar collector at angles β=35, β=40, and β=45. As is clear, for β=45, the maximum amount of radiation absorbed by the collector is at angles α_1=21 and α_2=21. For β=40, the maximum amount of radiation absorbed by the collector is at angles α_1=16 and α_2=26, and for β=35, it is at α_1=11 and α_2=32. The observed variation in optimal reflector angles with collector tilt angle (β) can be explained by the geometric relationship between incident solar rays, reflector orientation, and absorber surface alignment. As β increases, the angle at which direct solar radiation impinges on the collector surface changes, thereby altering the effective reflection path required for redirected radiation to strike the absorber uniformly. The lower reflector (α_1) primarily enhances irradiation during lower solar altitude angles, while the upper reflector (α_2) becomes more effective at higher sun elevations. Consequently, the optimal reflector configuration represents a balance between minimizing reflection losses and maximizing overlap between reflected rays and the absorber surface. These results highlight the importance of adaptive or seasonally adjustable reflector angles to sustain enhanced solar interception under varying installation tilt angles and solar positions.

4.3. Effect of Collector Area on Key Performance Parameters

Fig. 8 displays the effect of solar collector area on the feed outlet temperature (T_f) and PVT module temperature (T_{tpv}) throughout the day. From 8:00 to approximately 13:00, T_f exhibits an increasing trend due to rising solar irradiance. After reaching a peak near 13:00, T_f decreases as irradiance declines. A larger collector area results in higher T_f, with the maximum value observed at A = 2 m² compared to A = 1.5, 1.0, and 0.5 m². This is attributed to the greater amount of thermal energy absorbed as the collector area increases. A similar trend is observed for T_{tpv} (Fig. 8), where the highest values are again obtained at A = 2 m².

Fig. 9 presents the influence of collector area on electrical power output (P_{tpv}) and electrical efficiency. As expected, P_{tpv} increases with collector area and peaks around solar noon due to higher irradiance and absorbed energy. Conversely, electrical efficiency decreases with increasing collector area and operating temperature (T_{tpv}). This behavior aligns with the

well-known temperature dependence of photovoltaic efficiency: higher T_{tpv} reduces η_{tpv}, despite the increase in absorbed energy.

Fig. 10 shows that both thermal efficiency and overall energy efficiency decrease with increasing collector area and time of day. Although a larger area increases useful thermal energy (Eq. 5), it simultaneously raises operating temperatures, thereby increasing heat losses to the surroundings (Eq. 12). This trade-off highlights the necessity of optimizing collector area to maximize freshwater production (Fig. 11) without excessively compromising overall system efficiency. Although increasing the collector area significantly enhances useful thermal energy absorption, it also intensifies heat losses to the surroundings. As the absorber and storage tank operate at higher temperatures for larger areas, convective and radiative losses from the glass cover and absorber surface increase, as described by Eqs. (10)–(12). Additionally, larger areas raise the mean fluid temperature within the storage tank, thereby amplifying thermal losses through the tank insulation. As a result, despite the increase in absolute thermal energy gained, the ratio of useful energy to total incident solar energy decreases, leading to a reduction in both thermal efficiency and overall system efficiency. This behavior explains the apparent contradiction between higher freshwater productivity (Fig. 11) and lower efficiency values observed in Fig. 10.

Fig. 11 reveals that daily freshwater production rises significantly from 6.4 kg/day at A = 0.5 m² to 54.1 kg/day at A = 2 m². This enhancement is directly linked to the higher feed temperature (T_f, Fig. 8), which increases the vapor pressure difference across the membrane ($P_{m,f} - P_{m,p}$, Eq. 14), thereby augmenting mass flux (J, Eq. 13). A larger collector area supplies more thermal energy, facilitating greater vapor transport. However, as later shown in Fig. 15, increasing coolant flow rate has an opposite effect by reducing T_f, emphasizing the critical balance required between collector area and flow rate to maximize distillate yield.

Table 2
Key design and operating parameters of the proposed PVT–DCMD system

Component	Parameter	Symbol	Value / Range	Unit
PVT Collector	Collector area	A_C	0.5 – 2.0	m²
	Glass cover transmissivity	τ_g	0.96	–
Reflectors	Lower reflector angle	α_1	21	°
	Upper reflector angle	α_2	15	°

Component	Parameter	Symbol	Value / Range	Unit
Membrane Module (DCMD)	Membrane thickness	δm	100	µm
	Membrane porosity	ε	0.75	–
Operating Conditions	Feed mass flow rate	$\dot{m}_f$	0.003 – 0.005	$Kg.s^{-1}$
	Initial value of the tank water temperature	T_{fi}	29	°C

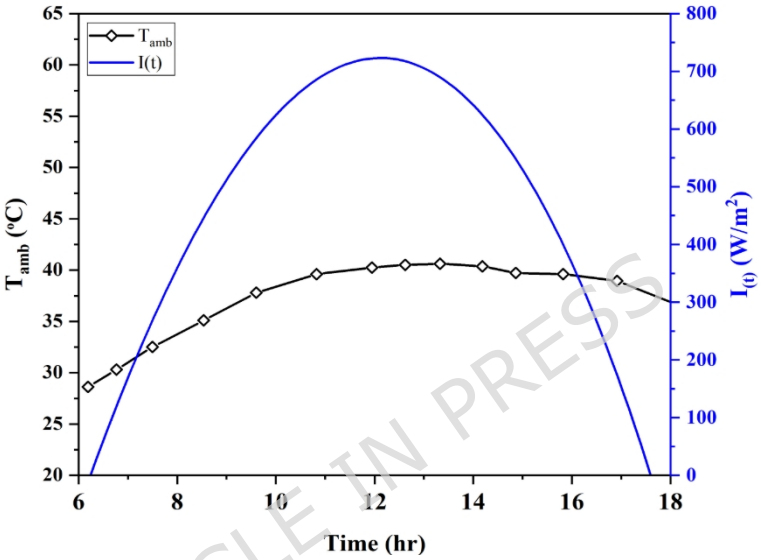

Fig. 4. Solar irradiance and ambient temperature profiles [24]

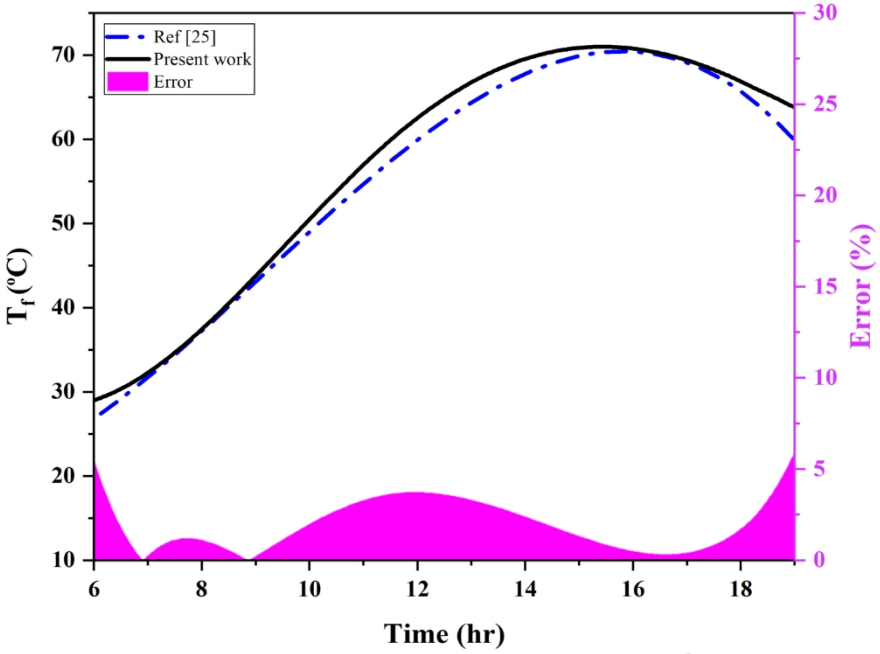

Fig. **5**. Validation of the photovoltaic-thermal system [25]

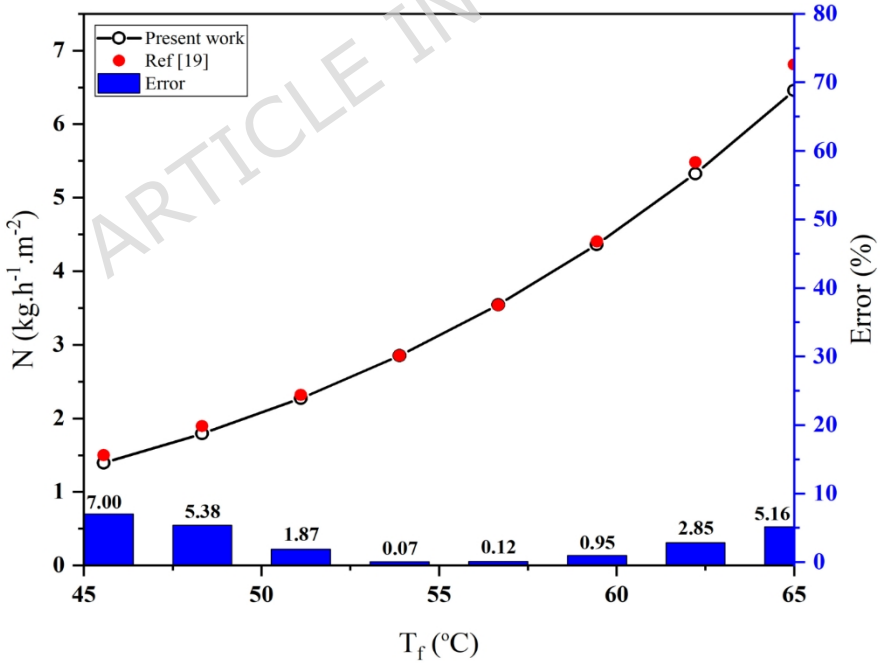

Fig. 6. Validation of the DCMD system [19]

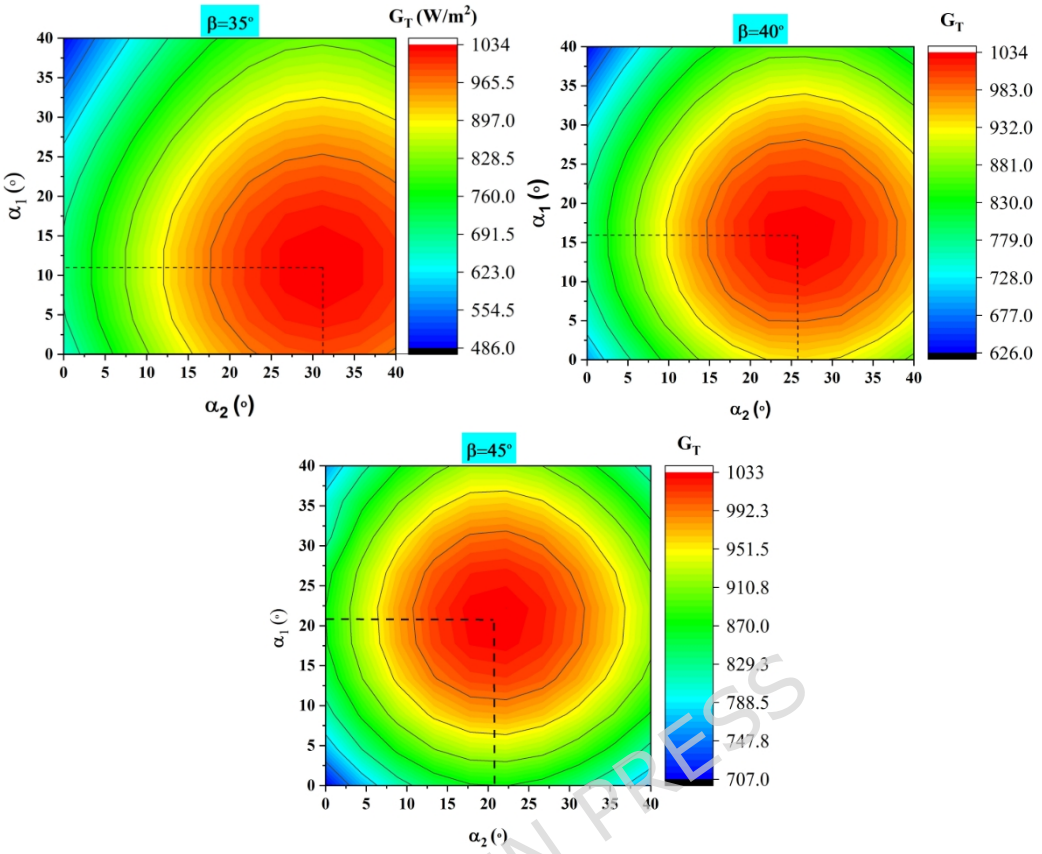

Fig. **7**. Effect of reflector angles on total absorbed solar radiation

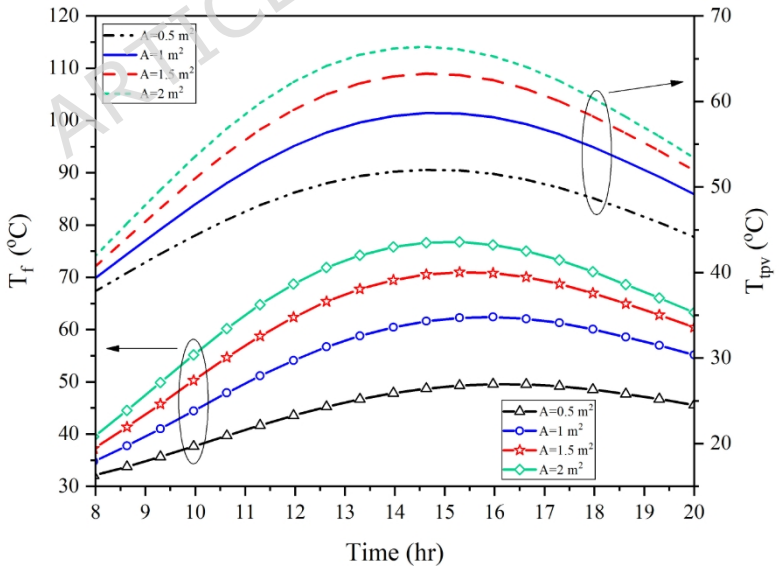

Fig. 8. Influence of collector area on T_f and T_{tpv} throughout the day

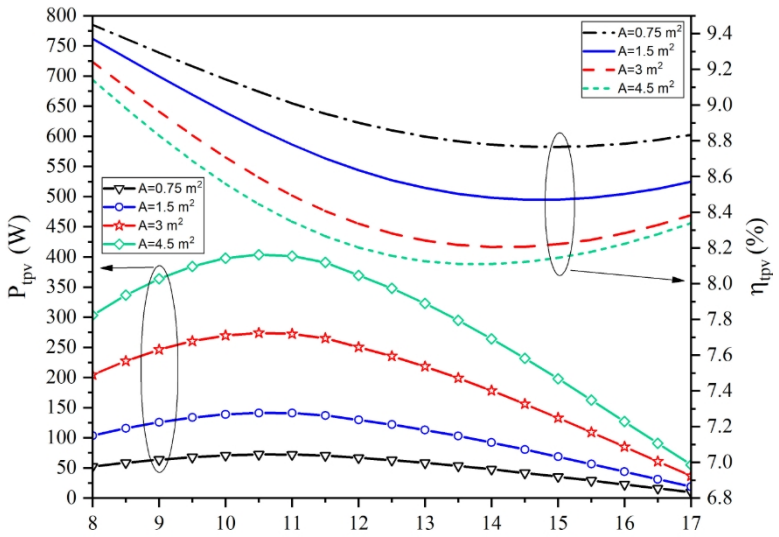

Fig. 9. Influence of collector area on electrical power and electrical efficiency

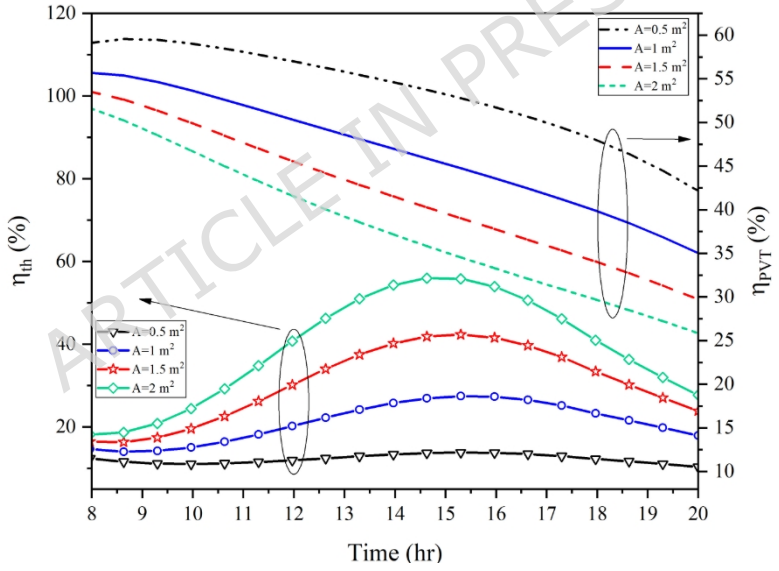

Fig. 10. Thermal and overall energy efficiency versus collector area

4.4. Effect of Feed/Coolant Flow Rate on Key Performance Parameters

Fig.12 illustrates the influence of feed flow rate on the feed outlet temperature (T_f) and PVT module temperature (T_{tpv}). As the flow rate increases from 0.003 to 0.005 kg/s, both T_f and T_{tpv} decrease throughout the day. The highest temperatures are obtained at the lowest flow rate (0.003 kg/s). This occurs because a higher flow rate extracts more heat from the PVT collector, reducing the temperature rise of the circulating fluid for a fixed collector area of 1.5 m².

Fig. 13 shows that electrical power output (P_{tpv}) and electrical efficiency (η_{tpv}) increase with rising flow rate. This improvement is directly linked to the lower T_{tpv} achieved at higher flow rates (Fig. 12). Since photovoltaic efficiency is inversely related to cell temperature, enhanced cooling leads to higher electrical performance.

Fig. 14 reveals that both thermal efficiency (η_{th}) and overall energy efficiency (η_{PVT}) increase with coolant flow rate. This is attributed to the greater amount of useful thermal energy extracted from the PVT collector at higher flow rates, despite the lower outlet temperature.

Fig. 15 demonstrates the effect of flow rate on daily freshwater production. As the feed flow rate increases from 0.003 to 0.005 kg/s, daily distillate yield decreases from 18.7 kg/day to 10.2 kg/day. This reduction results from the lower feed temperature (T_f) delivered to the DCMD module (Fig. 12), which reduces the vapor pressure difference across the membrane ($P_{m,f} - P_{m,p}$, Eq. 14) and consequently lowers the transmembrane mass flux (J, Eq. 13).

This trend is opposite to the effect of collector area (Fig. 11), where larger areas increased production. The opposing influences of collector area and flow rate highlight a critical design trade-off: maximum freshwater production is achieved by combining a large collector area with a low feed flow rate, provided that the resulting higher T_f remains within the operational limits of both the PVT module and the DCMD system.

Based on the combined analysis of freshwater production and energy performance, an optimal operating window can be identified. For the investigated system, a collector area in the range of 1.0–1.5 m^2 provides a balanced compromise, ensuring sufficiently high freshwater production while avoiding excessive thermal losses that degrade overall efficiency. Similarly, a feed flow rate between 0.003 and 0.004 kg/s is recommended, as lower flow rates favor higher feed temperatures and distillate yield, whereas excessively high flow rates significantly reduce freshwater production despite improving electrical efficiency. Therefore, operating within these ranges enables a practical trade-off between maximizing water output and maintaining acceptable electrical and overall energy efficiencies.

From a practical perspective, the proposed PVT–DCMD system exhibits favorable scalability characteristics due to its modular architecture. The system can be readily expanded by increasing the number of PVT collector–DCMD modules operating in parallel, allowing adaptation to different freshwater demands without major redesign. In terms of cost implications, the absence of optical concentrators, sun-tracking mechanisms, vacuum systems, and multi-stage heat recovery significantly reduces capital and maintenance costs compared to more complex desalination configurations. The primary economic components are limited to standard flat-plate PVT collectors, commercial DCMD membranes, and basic pumping equipment, which are widely available and commercially mature. Nevertheless, several

real-world implementation challenges must be considered. These include membrane fouling and wetting under long-term operation with high-salinity feed water, performance degradation under dust accumulation and variable weather conditions, and the need for robust control of feed temperature to maintain optimal DCMD performance. In addition, land availability and water pre-treatment requirements may influence deployment feasibility in certain regions. Addressing these challenges through improved membrane materials, periodic cleaning strategies, and integrated thermal and electrical storage systems will be essential for successful large-scale and off-grid applications.

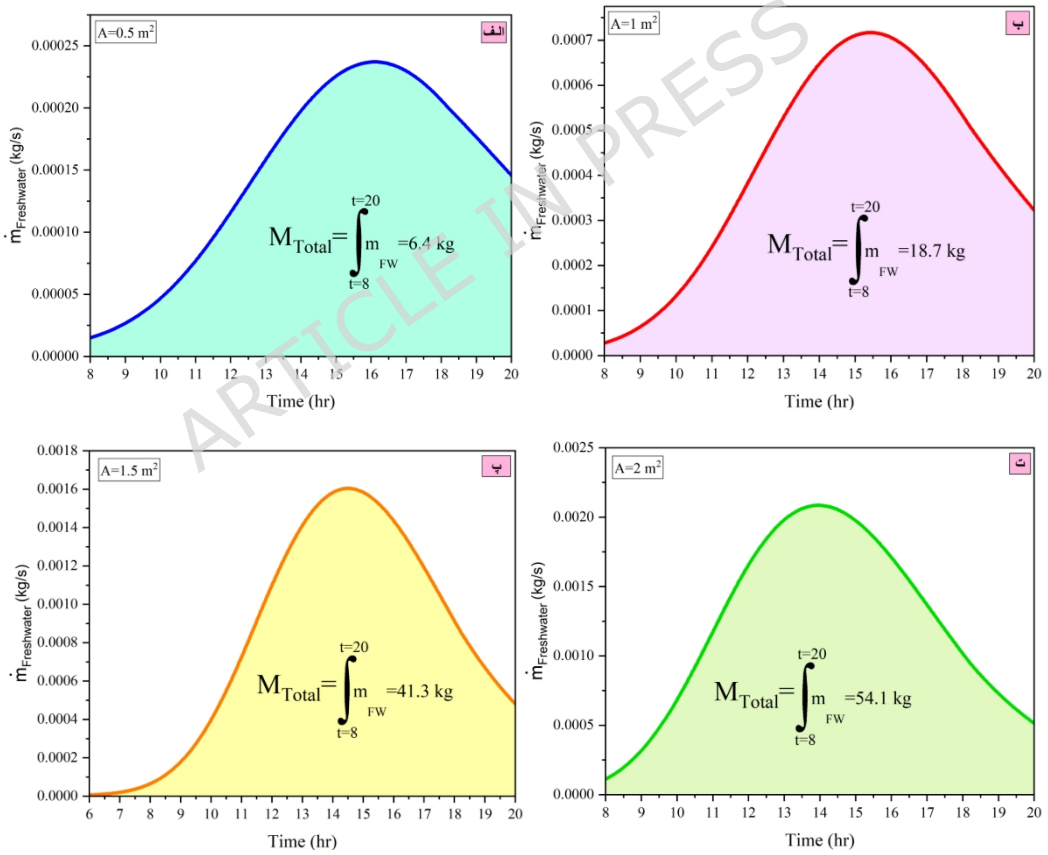

Fig. 11. Effect of PVT collector area on hourly and daily freshwater production

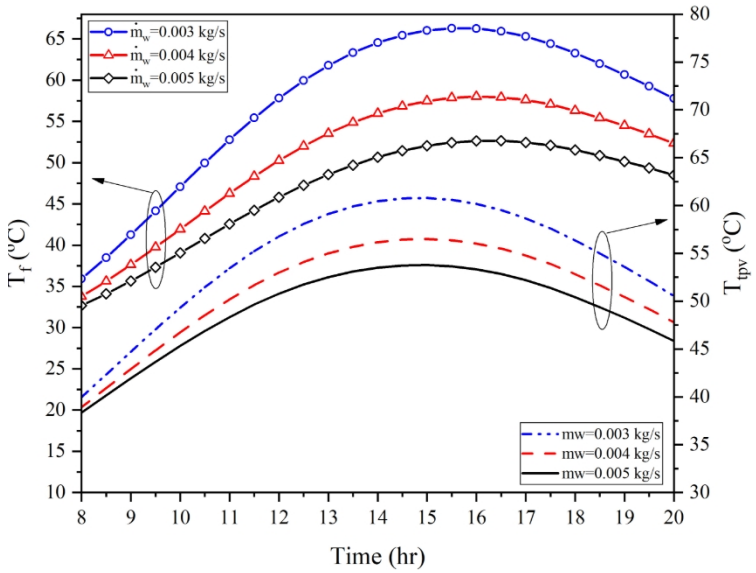

Fig. 12. Influence of feed flow rate on T_f and T_{tpv} throughout the day

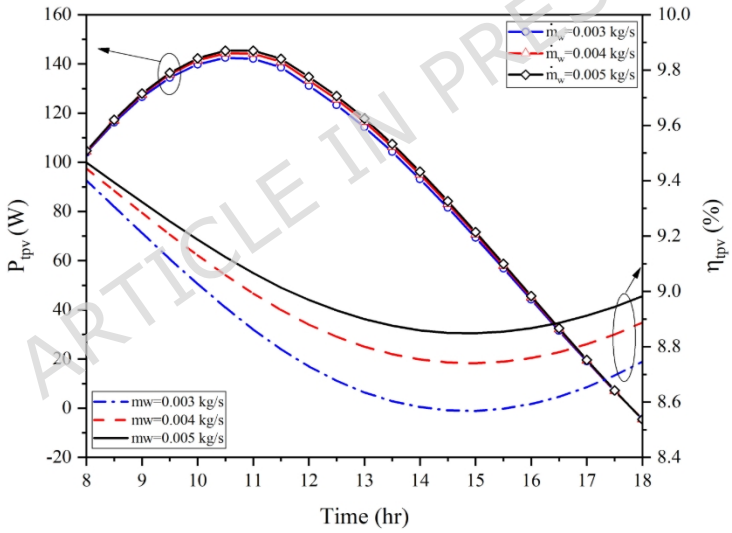

Fig. 13. Influence of feed flow rate on electrical power (P_{tpv}) and electrical efficiency (η_{tpv})

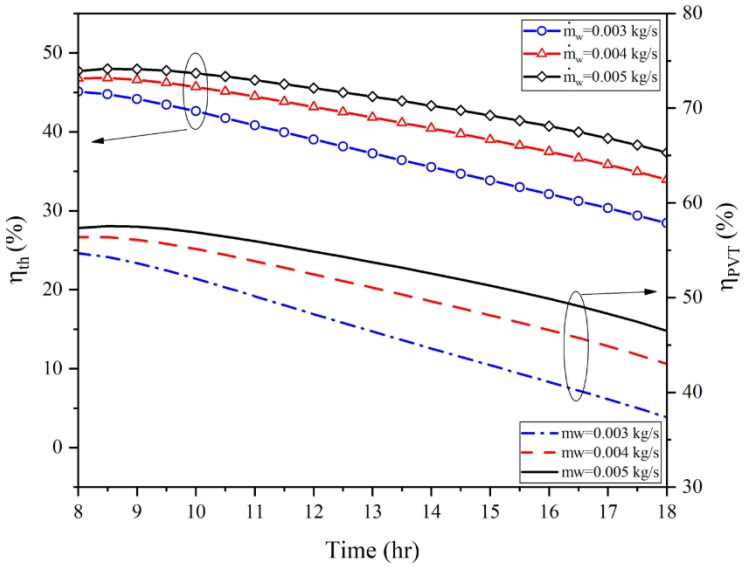

-Fig. 14. Influence of feed flow rate on thermal and overall energy efficiency

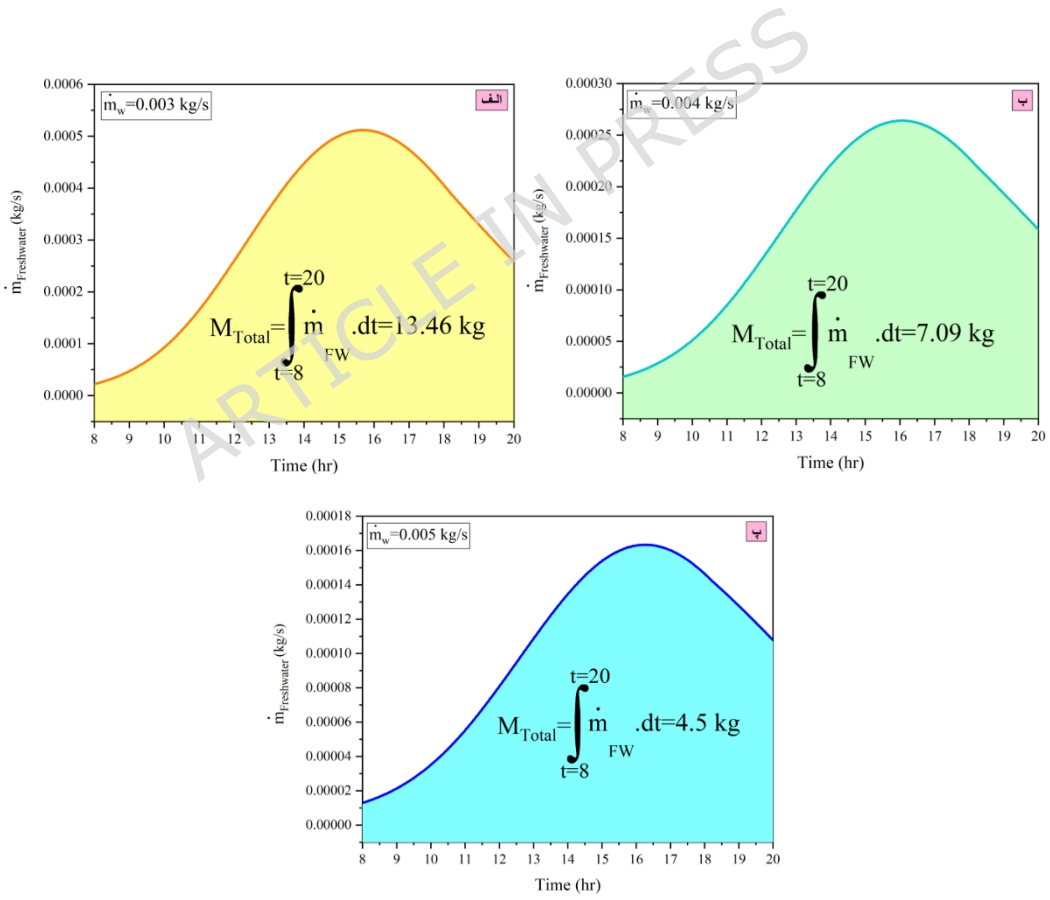

Fig. 15. Influence of feed flow rate on hourly and daily freshwater production

5. Comparison with Recent Studies

To assess the findings of this investigation within the broader field, the proposed setup, generating 18.7 kg of desalinated water each day, alongside a PVT thermal performance of 43.4% and total system energy utilization of 36.01 % amid typical sunlight patterns over an active surface of roughly 1m², was evaluated alongside prominent research efforts dating back to 2015. Criteria for inclusion emphasized overlapping designs, like channeling excess warmth from photovoltaic units to activate DCMD or AGMD setups, paired with quantifiable metrics on output volumes and operational yields. Table 3 outlines the key contrasts, with each referenced effort detailed below in a unified overview.

Table 3

Comparison of different systems with the current system in terms of thermal efficiency, total energy efficiency, and freshwater production.

Ref	System	Collector area (m^2)	Daily fresh water production (kg/day)	PVT thermal efficiency (%)	Total energy efficiency (%)	System complexity	Pros and Cons
Maqbool et al. [9]	Flat-plate PVT + DCMD	1.0~	۱۶–۱۲	۳۹–۳۵	۳۸–۳۲	Medium	No reflectors; annual-average analysis; steady-state assumptions
Al-Hrari et al. [26]	Concentrated PVT + DCMD	1.4~	۱۹–۱۵	۴۵–۴۱	71	High	Optical concentrator and sun tracking; high efficiency

							at the expense of cost and mechanical complexity
Wang et al. [27]	CPV + multi-stage DCMD	1.0~	١٨–١٠	–	٤١ تا	High	Multistage heat recovery; multiple pumps and control requirements
Present work	PVT+Reflectors+ DCMD	1.5	18.7	43.44	36	Low	No concentrator, no tracking, no vacuum system; transient outdoor simulation; simple and cost-effective design

Maqbool et al. [9] employed the TRNSYS platform to simulate a flat-panel PVT paired with DCMD across a full-year cycle, attaining 12–16 kg/day water generation and a combined energy yield of 32– %38across a 1m² footprint. A core asset was the extended evaluation incorporating authentic climate data from diverse urban settings, fostering a robust view of seasonal shifts. That said, the monthly averaging method bypassed hourly irradiance swings and overlooked impacts from panel orientations or supplementary mirrors, which likely led to conservative estimates of real-time and cumulative daily outputs.

Al-Hrari et al. [26] merged a focused photovoltaic-thermal (CPV/T) array with DCMD through rigorous lab trials, securing 15– 19kg/day production (over 1.4m²) and thermal yields between 41–%45. The standout feature was leveraging intensified light gathering, which amplified energy capture under intense exposure. On the downside, deploying Fresnel optics alongside sun-following mechanisms drove up startup expenses and mechanical intricacies considerably.

Wang et al. [27] harnessed the excess heat from conventional photovoltaic panels to drive multi-stage MD setups, achieving notably high thermal efficiencies exceeding 40% and fresh water yields reaching up to 18 kg/day under laboratory conditions. The main advantage stemmed from effective multi-stage heat recovery, which maximized energy reuse. Nevertheless, the reliance on several pumps, supplementary flow paths, and precise regulation of temperature and pressure levels increased system intricacy, raised fabrication and upkeep expenses, and heightened vulnerability to scaling. Consequently, such arrangements prove less practical for compact deployments or rural settings.

Placement of the Current Investigation Among These Efforts The configuration advanced here, steering clear of focusing elements or elaborate multi-phase builds, relied solely on a conventional flat-panel PVT enhanced by paired side-mounted adjustable mirrors to realize 18.7kg daily desalinated output and 43.4 % thermal yield in genuine field scenarios—figures that align with or surpass the bulk of the aforementioned cases. Moreover, the exhaustive transient framework within the Engineering Equation Solver (EES) setting, which jointly probes collector inclination, paired mirror alignments, and input stream velocity, complemented by hourly snapshots of thermal levels and yield curves across daylight hours, marks elements underexplored in totality by the benchmarked research.

It should be noted that reported values of total energy efficiency in the literature are strongly dependent on the adopted definition, system boundaries, and operating assumptions. In several studies reporting unusually high total efficiencies (exceeding 60–70%), the efficiency is often calculated by summing thermal and electrical outputs without consistently accounting for auxiliary losses, transient effects, or the latent heat contribution associated with freshwater production. Moreover, some investigations are conducted under steady-state or laboratory-controlled conditions with concentrated solar input, which can significantly inflate efficiency values compared to real outdoor transient operation.

In the present work, the total energy efficiency is evaluated using a conservative and physically consistent formulation that simultaneously accounts for electrical power generation, useful thermal energy, and the latent heat of freshwater production under realistic transient solar conditions. As a result, the obtained total efficiency of 36.01% represents a more practical and reliable performance indicator for real-world, off-grid applications, rather than an upper-bound or idealized value.

Additionally, systems reporting higher total efficiencies often employ optical concentrators, multi-stage heat recovery, or controlled indoor

environments, which enhance energy utilization but introduce higher complexity and cost. In contrast, the proposed system prioritizes simplicity, affordability, and operational robustness, leading to moderate yet realistic efficiency values that are more suitable for decentralized and rural implementations.

Taken together, these results illustrate how the suggested approach delivers comparable or enhanced results relative to recent, often more intricate and costly options, all while prioritizing straightforward design and affordability. It emerges as a practical choice for dual-purpose water and power supply in underserved rural settings with reliable sunlight.

6. Conclusions

In the present study, a solar-driven cogeneration system integrating a photovoltaic-thermal (PVT) collector with a DCMD unit was numerically investigated from an energy perspective. The proposed system simultaneously produces electricity and freshwater using only renewable solar energy.

Under baseline operating conditions and a collector area of 1.5 m^2, the system yields 18.7 kg/day of freshwater. At peak solar irradiance (around 13:00), the overall energy efficiency of the integrated system reaches 36.01%, while the instantaneous electrical power output of the PVT module is 113 W.

The parametric analysis revealed the following key trends:

- Increasing the solar collector area leads to higher feed temperature (T_f), PVT module temperature (T_{tpv}), electrical power output (P_{tpv}), and daily freshwater production. However, electrical efficiency (η_{tpv}), thermal efficiency (η_{th}), and overall energy efficiency (η_{PVT}) exhibit a decreasing trend due to elevated operating temperatures and increased heat losses.
- Increasing the feed flow rate through the PVT collector reduces T_f, T_{tpv}, and consequently daily freshwater production, while improving electrical power (P_{tpv}), electrical efficiency (η_{tpv}), thermal efficiency (η_{th}), and overall energy efficiency (η_{PVT}) as a result of enhanced cooling of the photovoltaic cells and greater extraction of useful thermal energy.

These opposing effects underline the existence of an optimal trade-off between collector area and coolant flow rate: maximum freshwater production is favored by large collector areas combined with low flow rates,

whereas maximum electrical and overall energy efficiency is achieved with high flow rates. The findings demonstrate that the proposed PVT-DCMD cogeneration system offers a promising, sustainable solution for decentralized water and electricity supply in regions facing simultaneous energy and water scarcity.

Overall, this work advances previous PVT–MD research by presenting the first fully transient daily performance analysis that simultaneously incorporates reflector-angle optimization and a coupled thermal–electrical–desalination trade-off assessment within a unified PVT–DCMD framework. This integrated perspective provides deeper design insight than steady-state or single-objective studies and supports more informed optimization of solar-driven cogeneration systems.

7. Future Work

Future research will focus on extending the present work toward a comprehensive techno-economic and environmental assessment of the proposed PVT–DCMD system. In particular, a detailed economic analysis considering capital cost, operation and maintenance expenses, and levelized cost of freshwater is required to quantitatively evaluate the cost-effectiveness of the system under different climatic and demand scenarios. In parallel, a life-cycle emission assessment could be conducted to estimate potential reductions in greenhouse gas emissions resulting from the displacement of fossil-fuel-based desalination and electricity generation. Recent studies have highlighted the importance of integrating economic and environmental metrics when evaluating solar-driven desalination systems, demonstrating their significant impact on system feasibility and sustainability [28, 29]. Additionally, future work may investigate long-term operational aspects such as membrane fouling, system durability, and the integration of thermal or electrical energy storage to further enhance system reliability under real-world conditions.

Author contributions:

Ali Kiani Salavat: Methodology, Software, Data curation, Investigation, Writing – original draft.

Behrooz M. Ziapour: Conceptualization, Formal analysis, Supervision.

Data availability statement: The authors confirm that the data supporting the findings of this study are available within the article

Nomenclature

A_C	Collector area, (m^2)
A_{ins}	lateral area of the collector insulation, (m^2)
C_f	Specific heat of the water of tank, (J/(Kg K))
D_e	Overall diffusion coefficient
D_K	Knudsen diffusion term
D_M	Ordinary molecular diffusion term
G_{ref}	Intensity of solar radiation from reflector
h_f	Convective heat transfer coefficient between the absorber and the tank water, (W/(m^2 K))
h_{g_amb}	Convective heat transfer coefficient between the glass and ambient, (W/(m^2 K))
$h_{r\text{-}sky}$	Radiation heat coefficient between cover glass and sky, (W/(m^2 K))
I	Total solar intensity radiation on the collector, (W/(m^2))
J	Transmembrane permeate flux, ($kg \cdot m^{-2} \cdot s^{-1}$)
K_{abs}	Thermal conductivity of absorber surface, (W/(m K))
K_g	Thermal conductivity of cover glass, (W/(m K))
K_{ins}	Thermal conductivity of insulation, (W/(m K))
K_{sc}	Solar cell temperature, (_C)
L	Collector length, (m)
R_g	Universal gas constant, (J/mol.K)
T_{amb}	Ambient temperature, (^oC)
T_{bs}	Absorber back surface temperature, (^oC)
T_f	Tank water temperature, (^oC)
T_m	Mean temperature at the two membrane interfaces, (^oC)
T_{sc}	Solar cell temperature, (^oC)
U_{Loss}	Heat loss through the storage tank insulation, (W/(m^2 K))
U_T	An overall heat transfer coefficient from solar cell to absorber back surface, (W/(m^2 K))
$U_{tc,a}$	An overall heat transfer coefficient from solar cell to ambient through glass cover, (W/(m^2 K))
W	Width of PV module, (m)

Greek letters

α	Angle between horizontal plane and bottom reflector, (°)
α_{sc}	Solar cell absorbance

L_{abs}	Absorber surface thickness, (m)	β	Solar collector tilt angle, (°)
L_g	Cover glass thickness, (m)	β_{sc}	Solar cell packing factor
L_{ins}	Insulation thickness, (m)	ΔH_v	Latent heat required for phase change of water from liquid to vapor, (kJ/kg)
L_{sc}	Solar cell thickness, (m)	η_{PVT}	Total efficiency of PVT system
M_f	Water mass inside the storage tank, (Kg)	η_{SC}	Temperature dependent electrical overall efficiency
M_{WT}	Molar mass of water, (mol/gr)	$\eta_{th,PVT}$	Temperature dependent thermal overall efficiency
PD_{WA}	Binary diffusion coefficient of water vapor in air, (Pa·m²/s)	ρ_{al}	Reflectance from reflector plate
Pr	Dimensionless Prantel number	τ_g	Transmittance of the cover glass

References

[1] Ahmadi, H., Ziapour, B. M., Ghaebi, H., & Nematollahzadeh, A. (2024). Simulation of vacuum membrane desalination within an enhanced design of compact solar water heaters. Applied Thermal Engineering, 257, 124243. https://doi.org/10.1016/j.applthermaleng.2024.124243.

[2] Pourasl, H. H., Barenji, R. V., & Khojastehnezhad, V. M. (2023). Solar energy status in the world: A comprehensive review. Energy Reports, 10, 3474-3493. https://doi.org/10.1016/j.egyr.2023.10.022

[3] Cai, J., Fei, J., Li, L., Fei, C., Maghsoudniazi, M., & Su, Z. (2023). Multicriteria study of geothermal trigeneration systems with configurations of hybrid vapor compression refrigeration and Kalina cycles for sport arena application. Renewable Energy, 219, 119390. https://doi.org/10.1016/j.renene.2023.119390

[4] Bamasag, A., Almatrafi, E., Alqahtani, T., Phelan, P., Ullah, M., Mustakeem, M., ... & Ghaffour, N. (2023). Recent advances and future prospects in direct solar desalination systems using membrane distillation

technology. Journal of Cleaner Production, 385, 135737. https://doi.org/10.1016/j.jclepro.2022.135737
[5] Ahmadi, H., Ziapour, B. M., Ghaebi, H., & Nematollahzadeh, A. (2024). Optimization of vacuum membrane distillation and advanced design of compact solar water heaters with heat recovery. Journal of Water Process Engineering, 67, 106212. https://doi.org/10.1016/j.jwpe.2024.106212
[6] Nakoa, K., Rahaoui, K., Date, A., & Akbarzadeh, A. (2015). An experimental review on coupling of solar pond with membrane distillation. Solar Energy, 119, 319-331.
[7] Rahaoui, K., Ding, L. C., Tan, L. P., Mediouri, W., Mahmoudi, F., Nakoa, K., & Akbarzadeh, A. (2017). Sustainable membrane distillation coupled with solar pond. Energy Procedia, 110, 414-419. https://doi.org/10.1016/j.egypro.2017.03.162

[8] Pranto, M. M. H., Bari, Y. A., Mourshed, M., & Kibria, M. G. (2025). A comprehensive analysis of the PVT-integrated solar desalination technologies: Present condition, challenges and way forward. *Energy Nexus*, 100479. https://doi.org/10.1016/j.nexus.2025.100479

[9] Ali, A. S., & Bounahmidi, T. (2025). Design of PVT driven forward osmosis and membrane distillation pilot plant for co-production of water and electricity. *RSC advances*, *15*(8), 5751-5765. https://doi.org/10.1039/d4ra07525k

[10] Maqbool, F., Kumar, L., Soomro, M. I., & Harijan, K. (2025). Performance analysis and optimization of photovoltaic-thermal system with direct contact membrane distillation using metaheuristic algorithms. *Separation and Purification Technology*, *364*, 132488. https://doi.org/10.1016/j.seppur.2025.132488

[11] Maqbool F. , et al. (2024). Modeling and simulation of direct contact membrane distillation system integrated with a photovoltaic thermal for electricity and freshwater production. Frontiers in Energy Research. Volume 12 – 2024. https://doi.org/10.3389/fenrg.2024.1344214

[12] Laveet Kumar, Jahanzaib Soomro, Hafeez Khoharo, Mamdouh El Haj Assad. A comprehensive review of solar thermal desalination technologies for freshwater production[J]. AIMS Energy, 2023, 11(2): 293-318. https://doi.org/10.3934/energy.2023016

[13] Essa, M. E. S. M., El-sayed, H. S., El-kholy, E. E., Amer, M., Elsisi, M., Sajjad, U., ... & Awad, H. E. S. (2025). Developments in solar-driven desalination: Technologies, photovoltaic integration, and processes. *Energy Conversion and Management: X*, *25*, 100861. https://doi.org/10.1016/j.ecmx.2024.100861

[14] Lotfy, H. R., Staš, J., & Roubík, H. (2022). Renewable energy powered membrane desalination - review of recent development. *Environmental science and pollution research international*, *29*(31), 46552–46568. https://doi.org/10.1007/s11356-022-20480-y

[15] Jawed, A. S., Nassar, L., Hegab, H. M., van der Merwe, R., Al Marzooqi, F., Banat, F., & Hasan, S. W. (2024). Recent developments in solar-powered membrane distillation for sustainable desalination. *Heliyon*, *10*(11). https://doi.org/10.1016/j.heliyon.2024.e31656

[16] El Charif, Z., Hijazi, A., Cornu, D., & Bechelany, M. (2025). Enhancing water sustainability with direct contact membrane desalination: technological innovations and challenges. *Applied Water Science*, *15*(12), 312. https://doi.org/10.1007/s13201-025-02668-y

[17] Soomro, M. I., Kumar, S., Ullah, A., Shar, M. A., & Alhazaa, A. (2022). Solar-powered direct contact membrane distillation system: performance and water cost evaluation. *Sustainability*, *14*(24), 16616. https://doi.org/10.3390/su142416616

[18] Mahmoudi, F., Ng, D., Ang, K., & Xie, Z. (2024). Sustainable desalination through hybrid photovoltaic/thermal membrane distillation: Development of an off-grid prototype. *Solar Energy*, *284*, 113090. https://doi.org/10.1016/j.solener.2024.113090

[19] Ali, A. S., & Bounahmidi, T. (2025). Photovoltaic-thermal driven membrane distillation water desalination: Dynamic simulation in an actual weather condition. *Energy*, *324*, 135943. https://doi.org/10.1016/j.energy.2025.135943

[20] Ziapour, B. M., Alirezaei, H., & Ghorannevis, S. (2023). Energy recovery from the enclosures between the glassing covers in a compact photovoltaic thermal collector. Renewable Energy, 216, 119053. https://doi.org/10.1016/j.renene.2023.119053

[21] Ameen, N. A. M., Ibrahim, S. S., Alsalhy, Q. F., & Figoli, A. (2020). Highly saline water desalination using direct contact membrane distillation (DCMD):

experimental and simulation study. Water, 12(6), 1575. https://doi.org/10.3390/w12061575
[22] Khayet, M. (2011). Membranes and theoretical modeling of membrane distillation: A review. Advances in colloid and interface science, 164(1-2), 56-88. https://doi.org/10.1016/j.cis.2010.09.005
[23] Essalhi, M., & Khayet, M. (2013). Self-sustained webs of polyvinylidene fluoride electrospun nanofibers at different electrospinning times: 1. Desalination by direct contact membrane distillation. Journal of membrane science, 433, 167-179. https://doi.org/10.1016/j.memsci.2013.01.023
[24] Khalifa, A., Ahmad, H., Antar, M., Laoui, T., & Khayet, M. (2017). Experimental and theoretical investigations on water desalination using direct contact membrane distillation. Desalination, 404, 22-34. https://doi.org/10.1016/j.desal.2016.10.009
[25] Janajreh, I., Suwwan, D., & Hashaikeh, R. (2017). Assessment of direct contact membrane distillation under different configurations, velocities and membrane properties. Applied Energy, 185, 2058-2073. http://doi.org/10.1016/j.apenergy.2016.05.020
[26] Dubey S, Tiwari GN. Thermal modeling of a combined system of photovoltaic thermal (PV/T) solar water heater. Sol Energy 2008;82:602–12. https://doi.org/10.1016/j.solener.2008.02.005
[27] BM. Ziapour, V. Palideh, F. Mokhtari. (2016). Performance improvement of the finned passive PVT system using reflectors like removable insulation covers. App.Therm.Eng http://doi.org/10.1016/j.applthermaleng.2015.10.143
[28] Al-Hrari, M., Ceylan, İ., Nakoa, K., & Ergün, A. (2020). Concentrated photovoltaic and thermal system application for fresh water production. *Applied thermal engineering*, *171*, 115054. https://doi.org/10.1016/j.applthermaleng.2020.115054
[29] Wang, W., Shi, Y., Zhang, C. *et al.* Simultaneous production of fresh water and electricity via multistage solar photovoltaic membrane distillation. *Nat Commun* 10, 3012 (2019). https://doi.org/10.1038/s41467-019-10817-6
[30] Elminshawy, N. A., Diab, S., El-Damhogi, D. G., Yassen, Y. E. S., Ashoor, N. M., & Soliman, M. S. (2025). Assessment of a novel floating humidification-dehumidification desalination system utilizing an air sparging and submerged dehumidifier. *Desalination*, 119185. https://doi.org/10.1016/j.desal.2025.119185
[31] Elminshawy, N. A., Soliman, M. S., El-Damhogi, D. G., El-Nahhas, K., & Mujtaba, I. M. (2025). An innovative floating solar still equipped with a Fresnel lens and a submerging condenser: An experimental study. *Solar Energy*, *299*, 113807. https://doi.org/10.1016/j.solener.2025.113807